

A Control Model of Photovoltaic Flyback Grid Connected Inverter for Improving Current Quality

Tengfei Wei, Yuntao Zhang, Bingjing Gu, Cong Wang, Shuangjun Ding

Abstract—Photovoltaic flyback grid-connected microinverters are widely utilized. This paper first analyzes their working principle and establishes a small-signal model and an input ripple voltage model of the flyback grid-connected inverter. The small-signal model is nonlinear and time-varying. To optimize grid-connected current control, a control strategy based on the inverse method is proposed, transforming the original nonlinear time-varying system into a linear time-invariant system for control. When the flyback grid-connected inverter operates, ripple voltage is generated on its DC input, affecting the grid-connected current quality. This ripple voltage can be mitigated by improving the outer loop voltage control. Finally, an experimental prototype is built to compare results before and after improvement, validating the effectiveness of the proposed method in enhancing grid-connected current quality.

Index Terms—flyback grid-connected inverter, inverse method, nonlinear, time-varying system

I. INTRODUCTION

IN order to improve the efficient and high-quality use of energy and reduce pollution emissions, the proportion of renewable energy use should be increased. As a kind of green renewable energy, solar energy is inexhaustible, easy to implement, and has no pollution to the environment. As photovoltaic power generation technology matures, solar energy is being widely used as a renewable energy source [1]. Traditional centralized PV systems aggregate multiple PV panel arrays into grid-connected inverters for power generation. However, this configuration suffers from low generation efficiency, installation challenges, and panel mismatch issues [2]. The evolving trend in PV power

generation structures involves modular integration of connected inverters. Distributed power generation, recognized as the most ideal structure, ensures that when a PV module is shaded or its output power decreases, it does not affect the performance of other modules due to their independent operation. Consequently, distributed generation structures exhibit superior operational efficiency [3].

Microgrid-connected inverters are typically designed to feature simple structures, low costs, and high efficiency. They must also achieve maximum power point tracking (MPPT), voltage boosting, and inversion functionalities. As a result, microgrid-connected inverters are widely adopted in distributed PV power generation systems.

The flyback topology offers advantages such as minimal component count, structural simplicity, and electrical isolation [4-6], making it highly suitable for low-power grid-connected inverters. Previous studies have focused on enhancing the performance of flyback grid-connected inverters (FGCI) [7-8]. The small-signal model of FGCI is a nonlinear time-varying system with operating points that vary over time. Conventional grid-connected current control strategies often neglect this time-varying characteristic, leading to increased total harmonic distortion (THD) in the grid-connected current.

To address this issue, this paper proposes a grid-connected current control strategy based on the inverse method. First, a small-signal model of FGCI is established. Second, the nonlinear time-varying model is transformed into a linear time-invariant model using the inverse method, enabling effective grid-connected current control. Furthermore, this study investigates the impact of ripple voltage generated on the PV cell's DC bus during FGCI operation, which affects grid-connected current quality. The paper also explores the suppression of ripple voltage effects through improved outer loop voltage control.

II. WORKING PRINCIPLE OF FLYBACK GRID CONNECTED INVERTER

The FGCI demonstrates enhanced controllability in Discontinuous Conduction Mode (DCM), where power switches inherently operate as Zero Current Switches (ZCS), accounting for its predominant utilization in low-power applications. To optimize power conversion efficiency, the system is intentionally designed for sustained DCM operation.

Manuscript received September 27, 2024; revised April 16, 2025.

Tengfei Wei is an Associate Professor of the College of Electrical and Information Engineering, Lanzhou University of Technology, Lanzhou 730050, China. (corresponding author to provide phone: 15214027124; e-mail: tfwei@lut.edu.cn).

Yuntao Zhang is a graduate student of the College of Electrical and Information Engineering, Lanzhou University of Technology, Lanzhou 730050, China. (e-mail: 3186025985@qq.com).

Bingjing Gu is a Senior Technician at Lanzhou Lanshi Group Co., Ltd., Lanzhou 730050, China. (e-mail: 2845594403@qq.com).

Cong Wang is a graduate student of the College of Electrical and Information Engineering, Lanzhou University of Technology, Lanzhou 730050, China. (e-mail: 1346794179@qq.com).

Shuangjun Ding is an Engineer at China Energy Construction Group Investment Co., Ltd., Henan Branch, Zhengzhou, 450000, China. (E-mail: 2806892555@qq.com).

The topology of FGCI is illustrated in Fig. 1. The flyback converter topology provides dual functionality, offering both electrical isolation and voltage boost capabilities. Subsequently, an H-bridge configuration serves as the inverter stage. A post-stage filter is incorporated to attenuate high-frequency harmonic components generated by switching operations in the grid-connected current, ensuring compliance with power quality standards.

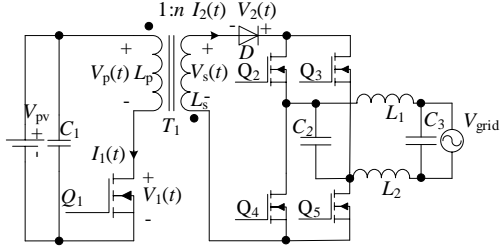


Fig. 1. Topology of FGCI.

Comparing the H bridge with grid voltage V_{grid} as a sinusoidal half-wave V_g , Fig. 1 can be simplified to Fig. 2.

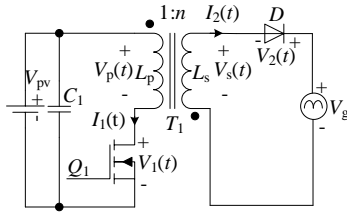


Fig. 2. Simplified FGCI topology.

In Fig. 2, $V_1(t)$ is the voltage across DS of MOSFET Q_1 . $V_2(t)$ is the voltage across the cathode and anode of diode D . $I_1(t)$ is the current flowing through primary transformer T_1 . $I_2(t)$ is the current flowing through the secondary transformer T_1 . V_{pv} is the voltage of a photovoltaic panel. $V_g(t)$ is sine half-wave voltage. n is the ratio of secondary to primary of T_1 . L_p is the primary inductance of T_1 . L_s is the secondary inductance of T_1 . $V_p(t)$ and $V_s(t)$ are respectively primary and secondary voltages of T_1 .

To make FGCI work in DCM mode, the following condition is guaranteed in design:

$$D_1^{\max} \left(1 + \frac{nV_{\text{pv}}^{\min}}{V_g^{\max}}\right) < 1 \quad (1)$$

In Equation (1), D_1^{\max} is the maximum duty of conduction of Q_1 , V_{pv}^{\min} is the minimum voltage of the photovoltaic panel. V_g^{\max} is the maximum voltage of V_g .

Waveforms of voltage and current of FGCI in steady-state operation are shown in Fig. 3. In Fig. 3, i_p is the peak current of primary T_1 . T is a switching period. FGCI is divided into three working states in one switching cycle. Analysis of each working state is as follows:

A. State 1(t_0-t_1):

In Fig. 2 and Fig. 3, at the time t_0 , Q_1 is turned on at ZCS, V_{pv} is applied to primary inductance L_p of T_1 , and $I_1(t)$ of primary of T_1 is increased linearly. When V_{pv} and primary

inductance L_p of T_1 is constant, a maximum current of $I_1(t)$ is related to the time when Q_1 is turned on. D is reversed and the secondary side of T_1 does not output power. At this time, voltage and current in the topology of FGCI are shown as state 1 in Table I.

TABLE I
VOLTAGE AND CURRENT IN TOPOLOGY

State	$V_1(t)$	$V_2(t)$	$I_1(t)$	$I_2(t)$
State1(t_0-t_1)	0	$V_g(t)+nV_{\text{pv}}$	$V_{\text{pv}}t/L_p$	0
State2(t_1-t_2)	$V_g(t)/n+V_{\text{pv}}$	0	0	$-V_g(t)/L_s+V_p$ $v_{t_1}/(nL)$
State3(t_2-T)	V_{pv}	0	$V_g(t)$	0

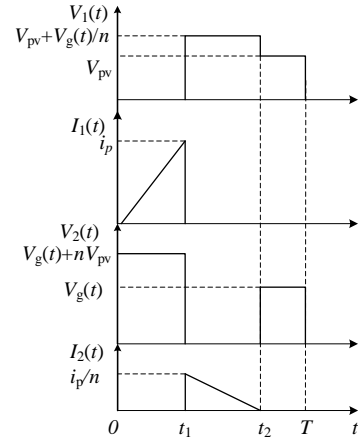


Fig. 3. Waveforms of voltage and current in FGCI.

B. State 2(t_1-t_2):

In Fig.2 and Fig.3, at the time t_1 , Q_1 is turned off, and energy is stored in the primary inductance L_p of T_1 . $I_2(t)$ in secondary inductor L_s flows through the D and is fed to V_g . Since voltage V_s is clamped by V_g , $I_2(t)$ of secondary of T_1 decreases linearly. At this time, voltage and current in the topology of FGCI are shown as state 2 in Table I. Here, t_1 is the conduction time of Q_1 .

C. State 3(t_2-T):

As illustrated in Figs. 2 and 3, the secondary current $I_2(t)$ of transformer T_1 demonstrates a linear decrease, attaining zero at time t_2 , thereby transitioning diode D into the off state. This operational mode aligns with State 3 in Table I, characterizing the voltage and current profiles of the FGCI topology during this phase.

III. SMALL SIGNAL MODELING OF FLYBACK INVERTER

FGCI uses constant switching frequency, so an average switching period and small signal disturbance method can be used to establish the small signal model of FGCI.

Through the above analysis of the working principle of FGCI, in one switching cycle, the four variables $V_1(t)$, $I_1(t)$, $V_2(t)$, and $I_2(t)$ are averaged. Then there are:

$$\overline{V_1(t)} = (1 - D_1(t))V_{\text{pv}}(t) + \frac{V_g(t)}{n}D_2(t) \quad (2)$$

$$\overline{I_1(t)} = \frac{1}{T} \int_0^{D_1(t)T} \frac{V_{pv}t}{L_p} dt = \frac{V_{pv}T}{2L_p} D_1^2(t) \quad (3)$$

$$\overline{V_2(t)} = (1 - D_2(t))V_g(t) + nV_{pv}(t)D_1(t) \quad (4)$$

$$\begin{aligned} \overline{I_2(t)} &= \frac{1}{T} \int_{D_1(t)T}^{(D_1(t)+D_2(t))T} \left[\frac{-V_g}{n^2L_p}t + \frac{D_1T(V_g + nV_{pv})}{L_s} \right] dt \\ &= \frac{D_2T}{2nL_pL_s} [2D_1(L_sV_{pv} - L_pV_gn) - D_2L_pV_gn] \end{aligned} \quad (5)$$

Equation (2), $\overline{V_1(t)}$ represents the average value of $V_1(t)$ over one switching cycle, where D_1 denotes the duty cycle of Q_1 , satisfying $t_1 = D_1T$. Similarly, D_2 corresponds to the duty cycle of D , with $t_2 - t_1 = D_2T$, where t_2 indicates the turn-off instant of D . Equation (3) defines $\overline{I_1(t)}$ as the average primary current of T_1 per switching cycle. Equation (4) expresses $\overline{V_2(t)}$ the average voltage across D during a switching cycle, while Equation (5) specifies $\overline{I_2(t)}$ the average secondary current of T_1 per switching cycle.

D_2 is obtained from (6) and is shown in (7).

$$\frac{V_{pv}}{L_p} D_1T = \frac{nV_g}{L_s} D_2T \quad (6)$$

$$D_2 = \frac{nV_{pv}}{V_g} D_1 \quad (7)$$

L_p and L_s have the following relationship:

$$L_s = n^2L_p \quad (8)$$

The relationship between duty D_1 of Q_1 and primary peak current I_p is as follows:

$$D_1 = \frac{L_p}{V_{pv}T} I_p \quad (9)$$

Bring (8) and (9) into (5), the relationship between $\overline{I_2(t)}$ and I_p is obtained as shown in (10).

$$\overline{I_2(t)} = \frac{L_s}{2n^2TV_g} I_p^2 \quad (10)$$

Small signal disturbance is added to $\overline{I_2(t)}$ and I_p in (10). Then (11) is obtained:

$$\overline{I_2} + \delta i_2 = \frac{L_s}{2n^2TV_g} (I_p + \delta i_p)^2 \quad (11)$$

By neglecting DC and higher-order harmonic components while retaining the small-signal terms in Equation (11), the

small-signal relationship between $\overline{I_2(t)}$ and I_p is derived as expressed in Equation (12):

$$F = \frac{\delta i_2}{\delta i_p} = \frac{L_s I_p}{n^2 TV_g} \quad (12)$$

Equation (12) describes a nonlinear time-varying relationship involving two time-dependent parameters, $I_p(t)$ and $V_g(t)$. Due to the time-varying nature of the relationship between the small-signal component of $\overline{I_2(t)}$ and I_p , conventional control methods cannot be directly applied to design an optimal current controller for the FGCI, potentially leading to degradation in grid-connected current quality.

IV. MODELING INPUT RIPPLE VOLTAGE OF FLYBACK INVERTER

The operation of the FGCI induces ripple voltage on the input DC bus, which adversely affects the quality of the grid-connected current. To analyze this phenomenon, it is essential to investigate the ripple voltage characteristics. Specifically, a small-signal relationship between the ripple voltage and the grid-connected power must be established. Based on Equations (3) and (9), the relationship between $\overline{I_1(t)}$ and I_p can be derived as follows.

$$\overline{I_1(t)} = \frac{L_p}{2V_{pv}T} I_p^2 \quad (13)$$

By introducing small-signal perturbations to $\overline{I_1(t)}$ and I_p in Equation (16), the resulting relationship is expressed in Equation (17):

$$\overline{I_1} + \delta i_1 = \frac{L_p}{2V_{pv}T} (I_p + \delta i_p)^2 \quad (14)$$

Equation (17) establishes the small-signal relationship between the input current and the primary peak current through the elimination of DC and higher-order harmonic components, retaining only the small-signal terms, as derived in Equation (18):

$$\frac{\delta i_1}{\delta i_p} = \frac{L_p I_p}{V_{pv}T} \quad (15)$$

Small signal relationship between ripple current δi_1 and current δi_2 of FGCI can be obtained by (12), (8), and (15) as shown below.

$$\delta i_1 = \frac{V_g}{V_{pv}} \delta i_2 \quad (16)$$

Since V_g and δi_2 are half-wave sinusoidal signals with time, it is known from (19) that the magnitude of ripple current δi_1 is affected by the above two terms.

$V_g \delta i_2$ Represents instantaneous grid-connected power. When δi_1 is a constant, the bigger the instantaneous grid-connected power is, the bigger the FGCI input ripple current δi_1 is, and the bigger ripple voltage on the capacitor C_1 of FGCI produced by δi_1 is.

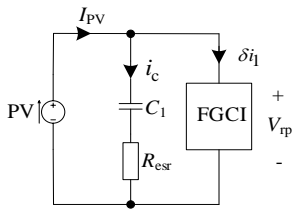


Fig. 4. FGCI input AC equivalent circuit.

Input AC equivalent circuit of FGCI is shown in Fig. 4. Photovoltaic cell has constant current characteristics, so the photovoltaic cell is equivalent to an ideal constant current source to simplify the analysis process, as shown PV in Fig. 4. i_c is currently flowing through input capacitor C_1 of FGCI. I_{pv} is the output current of photovoltaic panels. V_{tp} is the ripple voltage of the FGCI input. R_{esr} is equivalent series resistance of the capacitor C_1 . Because PV is equivalent to a constant current source, its impedance relative to the AC signal is infinite. According to Kirchhoff's current law, there is a relationship of (17).

$$I_{pv} = i_c + \delta i_1 \quad (17)$$

From (16) and (17) and δi_2 is substituted by I_g , following relations can be obtained.

$$i_c = I_{pv} - \frac{V_g}{V_{pv}} I_g \quad (18)$$

Add small signal perturbation to i_c and I_g in (18) to obtain (19):

$$i_c + \delta i_c = I_{pv} - \frac{V_g}{V_{pv}} (I_g + \delta I_g) \quad (19)$$

In (19), a small signal relationship between δi_c and δI_g is obtained by neglecting DC and higher-order components and taking a small signal part as shown in (20):

$$\delta i_c = -\frac{V_g}{V_{pv}} \delta I_g \quad (20)$$

Because i_c and I_g are AC signals, we can replace δi_c and δI_g use i_c, I_g them in (20) and get the following relationship.

$$i_c = -\frac{V_g}{V_{pv}} I_g \quad (21)$$

Set V_{g_RMS} and I_{g_RMS} be RMS of grid voltage and grid current respectively, and ω be angular velocity of grid AC voltage. Because grid-connected current and grid voltage has the same phase, the following equation can be used:

$$i_c = -\frac{2}{V_{pv}} V_{g_RMS} I_{g_RMS} \sin^2(\omega t) \quad (22)$$

The set P_{GP} is grid-connected power, so:

$$P_{GP} = V_{g_RMS} I_{g_RMS} \quad (23)$$

Then (22) can be simplified as follows:

$$i_c = -2 \sin^2(\omega t) \frac{P_{GP}}{V_{pv}} \quad (24)$$

(24) shows that when V_{pv} there is a fixed value, the larger grid grid-connected power P_{GP} of FGCI is, the larger i_c of C_1 is, and correspondingly the larger ripple voltage V_{tp} is produced by i_c on C_1 .

Then ripple voltage V_{tp} C_1 can be calculated as follows:

$$V_{tp}(s) = \frac{C_1 R_{esr} s + 1}{s^2 + 4\omega^2} \frac{P_{GP}}{V_{pv} C_1} \quad (25)$$

Inverse Laplacian transformation of (25) can be obtained:

$$V_{tp}(t) = \left(\frac{\sin(2\omega t)}{2C_1 \omega} + R_{esr} \cos(2\omega t) \right) \frac{P_{GP}}{V_{pv}} \quad (26)$$

(26) shows that ripple voltage V_{tp} is related to the grid-connected power P_{GP} of FGCI, the capacity of C_1 , the equivalent series resistance of C_1 , and voltage V_{pv} .

FGCI has grid-connected output power P_{GP} during operation, which is coupled to C_1 FGCI by equation (26) and produces ripple voltage V_{tp} , which produces ripple V_{tp_set} at I_{set} , as shown in Fig. 6.

V. CONTROL STRATEGY OF FLYBACK INVERTER

When a nonlinear time-varying system with parameter variations is transformed into a linear time-invariant (LTI) system, the control problem is reduced to that of an LTI system. This transformation enables the application of conventional control methodologies for controller design, thereby simplifying control system implementation while maintaining theoretical rigor. Such linearization facilitates streamlined controller synthesis through established techniques for LTI systems, effectively reducing computational complexity in practical applications.

is $P_{GP}=170W$. Peak to peak value V_{rp_Iset} is about 0.7V by introducing the above parameters into (30) and taking the inverse Laplace transform.

Adding BSF to the voltage outer loop is shown in Fig. 6. Transfer function of BSF is:

$$G_{BSF}(s) = \frac{s^2 + \omega_o^2}{s^2 + BW \cdot s + \omega_o^2} \quad (31)$$

It can be obtained by (25), (29) and (31). As shown in Fig. 6, ripple voltage V_{rp_Iset} is:

$$V_{rp_Iset}(s) = \frac{C_1 R_{esr} s + 1}{s^2 + 4\omega^2} \frac{P_{GP}}{V_{pv} C_1} K_P \left(1 + \frac{1}{K_I s}\right) \frac{s^2 + \omega_o^2}{s^2 + BW \cdot s + \omega_o^2} \quad (32)$$

To minimize the influence of BSF on the voltage outer loop, the notch bandwidth should be as small as possible. The notch bandwidth of BSF is $BW=3Hz$ and the center frequency is 100 Hz, so $\omega_o=200\pi$. Bringing the above parameters into (32) and taking the inverse Laplace transform, it is known that peak to peak value V_{rp_Iset} is about 0.18V. Compared with no BSF, the ripple voltage V_{rp_Iset} is reduced by about 4 times. Therefore, the THD of grid-connected current with BSF is smaller than nonuse BSF.

VI. EXPERIMENTAL RESULTS AND DISCUSSION

A. Experimental Parameters

To validate the above discussion, an experiment platform is established based on FPGA. The control strategy of grid-connected current is implemented using Verilog HDL. Therefore voltage outer loop control has a low sampling rate, and MPPT and BSF are implemented on ARM. The type of solar panel is a single crystal of UK-SOLAR. The maximum output power of the panel is 190 W, the open circuit voltage is 44.0 V, short circuit current is 5.68 A. Voltage at the maximum power point is 36 V, and at this time operating current is 5.28 A. Parameters of FGCI are shown in Table II.

Item	Parameters
Input DC voltage(V_{pv})	36V
Output maximum grid connection power	190W
Frequency(f)	100KHz
Transformer core material(A_L)	0.16 $\mu H/n^2$
Input and output dc capacitor(C_1)	18800 μF
Primary number of transformers(N_p)	5T
Secondary number of transformers(N_s)	30T
Turns ratio(n)	6
Primary inductance(L_p)	4 μH
Secondary inductance(L_s)	144 μH

B. Grid Connected Current Use Traditional PRI Control.

With the above parameters in Table II, the grid-connected current control block diagram is shown in Fig. 7. Grid-connected current control does not use the inverse method and only uses PRI control. The F of FGCI is

nonlinear and time-varying, as shown in (12). The peak value of I_{set} grid-connected current is 1.093A, and grid-connected power is 170W when the grid voltage is 220 V.

The grid-connected current waveform is shown in channel 2 of Fig. 8. Channel 1 is a grid voltage waveform V_{grid} , and channel 2 is grid grid-connected current waveform I_{grid} . At this time, the THD of grid-connected current is 14.3%.

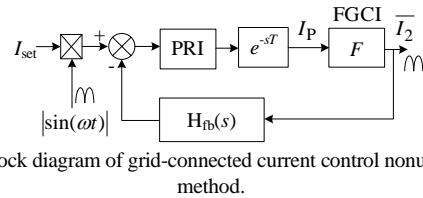


Fig. 7. Block diagram of grid-connected current control nonuse inverse method.

C. Grid Connected Current Use proposed Control based on the Inverse Method.

Using the same parameters in Table II, the control block diagram of the inverse method is shown in Fig. 5.

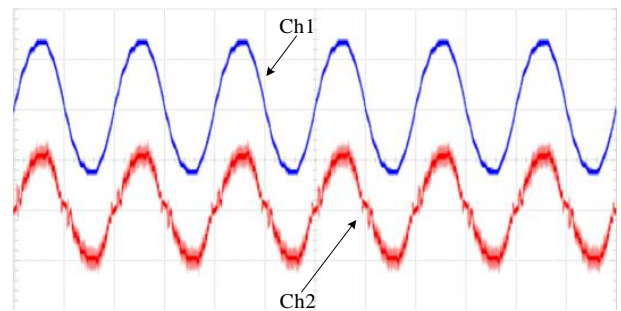


Fig. 8. Waveforms of V_{grid} and I_{grid} nonuse inverse method. Ch1, V_{grid} , 250V/div. Ch2, I_{grid} , 1A/div. time base, 10ms/div.

At this time, outer loop voltage control is not used, and only the current inner loop works. The peak value I_{set} of the grid-connected current is 1.093A and grid-connected power is 170W when grid voltage is 220 V.

The grid-connected current waveform is shown in Fig. 9. Channel 1 is a grid voltage waveform V_{grid} , and channel 2 is a grid current waveform I_{grid} . Grid-connected current can track the given value well in one grid cycle, and there is no obvious distortion near the zero crossing point I_{grid} . At this time, the THD of grid-connected current is 4.1%.

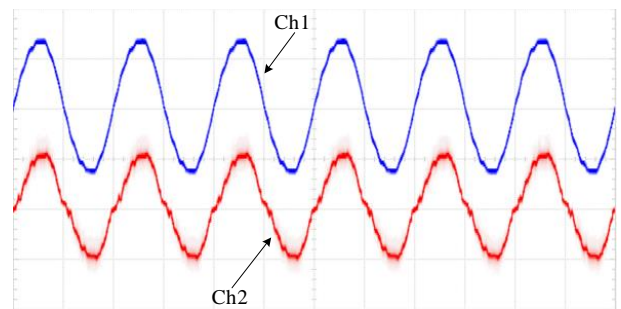


Fig. 9. Waveforms of V_{grid} and I_{grid} use the inverse method. Ch1, V_{grid} , 250V/div. Ch2, I_{grid} , 1A/div. time base, 10ms/div.

Comparing the FGCI grid-connected current waveform and THD of Fig. 8 and Fig. 9, it can be seen that the THD of grid-connected current using the inverse method is smaller

than without the inverse method. Then control strategy of grid-connected current based on the inverse method in FGCI can improve the quality of grid-connected current.

D. Current Quality of Outer Loop Voltage Control nonuse BSF

When the inverse method is used and BSF is not added to the outer loop voltage control, the experiment is performed using the above parameters. Grid-connected power is 170W and the RMS value of output current is 0.772A, grid-connected current waveform is shown in Fig. 10. Channel 1 is the grid voltage waveform V_{grid} , channel 2 is a grid-connected current waveform I_{grid} , channel 3 is the ripple voltage V_{rp} of the capacitor C_1 , and channel 4 is ripple voltage V_{rp_Iset} at I_{set} . At this time, the THD of grid-connected current is 5.5%.

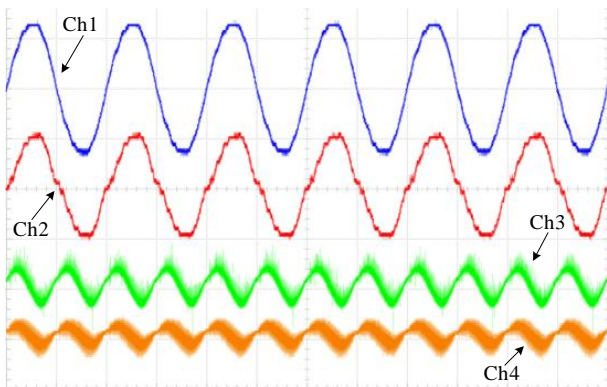


Fig. 10. Waveforms of V_{grid} , I_{grid} , V_{rp} , V_{rp_Iset} nonuse BSF. Ch1, V_{grid} , 250V/div. Ch2, I_{grid} , 1A/div. Ch3, V_{rp} , 1V/div. Ch4, V_{rp_Iset} , 1V/div. time base, 10ms/div.

E. Current Quality of Improved Outer Loop Voltage Control Use BSF

Under the same experimental conditions, BSF is added to the voltage outer loop control for the experiment. Experimental waveforms are shown in Fig. 11.

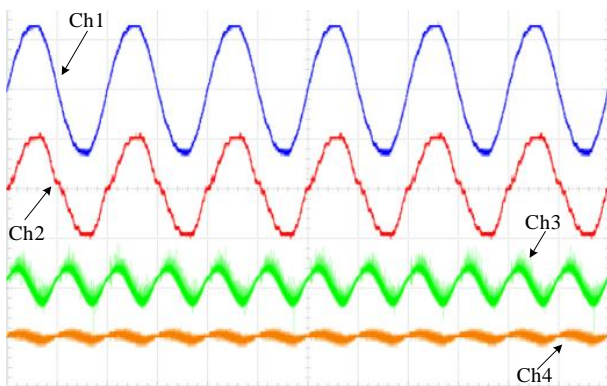


Fig. 11. Waveforms of V_{grid} , I_{grid} , V_{rp} , V_{rp_Iset} use BSF. Ch1, V_{grid} , 250V/div. Ch2, I_{grid} , 1A/div. Ch3, V_{rp} , 1V/div. Ch4, V_{rp_Iset} , 500mV/div. time base, 10ms/div.

Channel 1 is the grid voltage waveform V_{grid} , channel 2 is grid-connected current waveform I_{grid} , channel 3 is ripple voltage V_{rp} of capacitor C_1 , and channel 4 is ripple voltage

V_{rp_Iset} at I_{set} . It can be seen that the THD of grid-connected current waveform is better than nonuse BSF, and its THD is 4.3%.

A comparative analysis of grid-connected current THD with and without the BSF demonstrates that the enhanced voltage control outer loop significantly improves ripple voltage attenuation. This reduction in ripple voltage minimizes its impact on the grid-connected current, thereby further enhancing the overall current quality.

VII. CONCLUSION

This paper proposes a novel control method for the FGCI to enhance the quality of grid-connected current. The small-signal model of the FGCI, characterized as a nonlinear time-varying system, is transformed into a linear time-invariant system through an inverse method, enabling effective control. Experimental results demonstrate that the proposed method significantly improves grid-connected current quality and reduces THD. During FGCI operation, ripple voltage generated on the photovoltaic panel's DC bus interferes with the grid-connected current reference value, directly degrading its quality. To mitigate this, a BSF is integrated into the outer loop voltage control, effectively reducing the ripple's impact on the current reference. Experimental validation confirms that the BSF-enhanced control strategy improves grid-connected current quality. The proposed method extends the controllability of FGCI systems, facilitating their broader application in renewable energy systems.

REFERENCES

- [1] R. H. Wills, F. E. Hall, S. J. Strong, and J. H. Wohlgemuth, "The ac photovoltaic module," in *photovoltaic specialists conference*, pp. 1231-1234, 1996.
- [2] Q. Li and P. Wolfs, "A review of the single phase photovoltaic module integrated converter topologies with three different DC link configurations," *IEEE Transactions on Power Electronics*, vol.23, no.3, pp. 1320-1333, 2008.
- [3] S. B. Kjaer, J. K. Pedersen, and F. Blaabjerg, "Power inverter topologies for photovoltaic modules-a review," in *IEEE Industry Applications Society Annual Meeting*, pp. 782-788, 2002.
- [4] M. Gao, M. Chen, C. Zhang, and Z. Qian, "Analysis and implementation of an improved flyback inverter for photovoltaic ac module applications," *IEEE Transactions on Power Electronics*, vol.29, no.7, pp. 3428-3444 2014.
- [5] Suskis, Pavels; Galkin, Ilya; Zakis, Janis, "Design and implementation of flyback MPPT converter for PV-applications," *Electric Power Quality and Supply Reliability Conference*, 2014.
- [6] S. B. Kjaer, J. K. Pedersen and F. Blaabjerg, "A review of single-phase grid-connected inverters for photovoltaic modules," *IEEE Transactions on Industry Applications*, vol.41, no.5, pp. 1292-1306, 2005.
- [7] A. B. Shitole, S. Sathyan, H. M. Suryawanshi, G. G. Talapur and P. Chaturvedi, "Soft-switched high voltage gain boost-integrated flyback converter interfaced single-phase grid-tied inverter for spv integration," *IEEE Transactions on Industry Applications*, vol.54, no.1, pp. 482-493, 2018.
- [8] Kashyap, N.; Gautam, A., "Fault-tolerant peak current mode controlled flyback converter for solar PV modules," *International Conference on Power and Embedded Drive Control (ICPEDC)*, 2017.
- [9] Y. Zhang, M. M. Hendrix, and J. L. J. Duarte, "Observer-based mpc applied to flyback converters," in *International Power Electronics and Motion Control Conference*, pp. 337-341, 2016.
- [10] Y. Konishi, S. Chandhaket, K. Ogura and A. Nakaoka, "Utility-interactive high-frequency flyback transformer linked solar

- power conditioner for renewal energy utilizations," in *International Conference on Power Electronics and Drive Systems*, pp. 628-632, 2001.
- [11] A. C. Nanakos, E. C. Tatakis, and N. Papanikolaou, "A weighted-efficiency-oriented design methodology of flyback inverter for ac photovoltaic modules," *IEEE Transactions on Power Electronics*, vol.27, no.7, pp. 3221-3233, 2012.
- [12] T. Shimizu, K. Wada, and N. Nakamura, "A flyback-type single phase utility-interactive inverter with low-frequency ripple current reduction on the DC input for an AC photovoltaic module system," in *Power Electronics Specialists Conference*, pp. 1483-1488, 2002.
- [13] U. Yilmaz, A. Kircay and S. Borekci, "Pv system flyback converter controlled pi control to charge the battery under variable temperature and irradiance," *Electronics*, pp. 1-6, 2017.
- [14] H. Do, "A soft-switching dc/dc converter with a high voltage gain," *IEEE Transactions on Power Electronics*, vol.25, no.5, pp. 1193-1200, 2010.
- [15] S. Bircagalateanu, "Flyback converter output voltage stabilization," *IEEE Transactions on Aerospace and Electronic Systems*, no.2, pp. 146-151, 1987.